Heliyon 11 (2025) e40993

Contents lists available at ScienceDirect

Heliyon

journal homepage: www.cell.com/heliyon

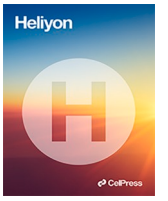

Research article

Preliminary mechanistic insights into the detection of ethanol vapour using MnO_2 NRs-CNPs-poly-4-(vinylpyridine) based solid-state sensor operating at room temperature

Lesego Malepe [a], Derek Tantoh Ndinteh [a], Patrick Ndungu [b], Messai Adenew Mamo [a,*]

[a] Department of Chemical Sciences, University of Johannesburg, PO Box 17011, Doornfontein, 2028, Johannesburg, South Africa
[b] Department of Chemistry, University of Pretoria, Private Bag X20, Hatfield, 0028, Pretoria, South Africa

ARTICLE INFO

Keywords:
Ethanol
Solid-state sensor
MnO_2 NRs
Polymer composites
Semiconductor metal oxide

ABSTRACT

Semiconductor metal oxide gas sensors are widely used to detect ethanol vapours, commonly used in industrial productions, road safety detection, and solvent production; however, they operate at extremely high temperatures. In this work, we present manganese dioxide nanorods (MnO_2 NRs) prepared via hydrothermal synthetic route, carbon soot (CNPs) prepared via pyrolysis of lighthouse candle, and poly-4-vinylpyridine (P4VP) composite for the detection of ethanol vapour at room temperature. MnO_2, CNPs, P4VP, and MnO_2 NRs-CNPs-P4VP composite were characterised using scanning electron microscopy, transmission electron microscopy, powder X-ray diffraction, Fourier transform infrared spectroscopy, and Raman spectroscopy. Five sensors were prepared, namely, sensor 1 ($MnO_{2\text{-NRs}}$), sensor 2 (CNPs), sensor 3 (CNPs-P4VP composite of a mass ratio of 1:3), sensor 4 (MnO_2 NRs-CNPs-P4VP composite of a mass ratio 1:1:3), and sensor 5 (MnO_2 NRs-CNPs-P4VP composite of a mass ratio 2:1:3). All the five sensors were used detect to 2-propanol, acetone, ethanol, methanol, and mesitylene vapours at room temperature, but among all the tested sensors, sensor 4 was highly sensitive to ethanol vapour and less sensitive to 2-propanol, methanol, acetone, and mesitylene vapours. The response and recovery time of sensor 4 towards ethanol vapour at 20.4 ppm were 82 seconds and 74 seconds, respectively. The limit of detection on ethanol vapour using sensor 4 was 789 ppb. During detection, the ethanol vapour undergoes total deep oxidation on the surface of sensor 4.

1. Introduction

Today, chemo resistive gas sensors gained huge attention over using hyphenated analytical instruments such as gas chromatography-mass spectroscopy to detect volatile organic compounds (VOCs) and environmental air monitoring [1,2]. Although it is possible to use analytical instruments for VOC detection, it is associated with high costs, long-time sample analysis, and requires a substantial amount of funds for maintenance; it needs trained personnel to operate, and most of the analytical instruments are bulky in size. Chemiresistive gas sensors measure the change in electrical resistance on the sensing element as it interacts with vapours or gases in outdoor or indoor environments [3]. These devices are used in gas detection because of their cost-effectiveness, portability, ease of

* Corresponding author.
E-mail address: messaim@uj.ac.za (M.A. Mamo).

https://doi.org/10.1016/j.heliyon.2024.e40993
Received 11 March 2024; Received in revised form 16 September 2024; Accepted 4 December 2024
Available online 11 December 2024

operation, ability to do online analysis, and shortening the analysis time. Ethanol gas sensors are in demand in many fields, including automobile industries, chemical industries, and car drunkard driver monitoring [4,5]. Ethanol is a VOC that vaporises easily at average air temperatures, typically >20 °C because of its high vapour pressure and low boiling point (78.4 °C) [6].

Semiconductor metal oxides (SMOs) such as titanium dioxide (TiO_2) [7], tin oxide (SnO_2) [8], and zinc oxide (ZnO) [9] are the mostly explored and studied materials in chemo resistive gas sensors due to their fast response, high sensitivity and are easy to synthesise them. However, they lack selectivity towards the targeted gas or VOC and also operate at extremely high temperatures over 150 °C [7–9]. MnO_2 is a semiconductor metal oxide often used in several applications: energy storage, water treatment, catalysis, and gas sensors. Preparing MnO_2 of different morphologies, dimensions, and particle sizes is easy. The differences in dimensions, particle sizes, and morphologies such as nanorods, nanosheets, nanoparticles exhibit unique chemical and physical properties [10–12]. MnO_2 exists in different crystallographic polymorphs namely, alpha (α), beta (β), gamma (γ) [13,14]. Okechukwu et al. reported α-MnO_2 nanorods (NRs) as one of the promising materials to be deployed in gas sensing applications, shown to have high sensitivity on VOCs [11]. In this work, we chose to use MnO_2 nanorods because they can operate at room temperature after being coupled with carbon-based material [11] and having a sensor that operates at room temperature saves the high costs of the current sensors that operate at extremely high temperatures, resulting in high energy consumption.

The inexpensive carbon nanoparticles (carbon soot) (CNPs) are introduced into MnO_2 NRs to allow the MnO_2-based sensors to operate at room temperature. Similar findings were reported wherein carbon additives drop the high working temperature of pure semiconductor materials in gas sensors [15–18]. The carbon nanoparticles improve the electrical conductivity of MnO_2 NRs, enhancing response-recovery times and high sensitivity [11,12,14]. The carbon soot was previously utilised in gas sensing and showed some interactions towards the VOCs, although it showed small responses working at room temperature, which is the main reason why we opted to utilise the material to make a composite. The pyrolysis of candles in atmospheric air is a simple method to synthesise carbon nanoparticles (soot) and is used to detect VOCs at room temperature; however, they have slow response, poor selectivity, and sensitivity [14].

In addition to MnO_2 and carbon soot, Poly-4-(vinylpyridine) (P4VP) was one of the materials that was utilised to make a gas-sensing composite. Polymers have been deployed as additive materials to improve sensitivity. P4VP is a linear hydrocarbon chain containing a pyridine compound. Pyridine is a six-membered ring heterocyclic organic compound containing five carbons, five hydrogens, and one nitrogen atom, C_5H_5N. P4VP is the most common polyvinylpyridine type used in many applications, including sensors, batteries, and supercapacitors, because of its high electrical conductivity and fast electron transferability [19,20]. In P4VP, the pyridine is attached to a linear hydrocarbon chain on its para-position. The P4VP works as a binder in the composite. It has high electron π delocalisation, which could be why a synergic effect is usually observed when polymers are used as additive materials. A work reported by B. Yoon et al., reported single-walled carbon nanotube (SWCNT): poly-4-vinyl pyridine (P4VP) gas sensor for gas detections, and P4VP was used as an additive into SWCNT and synergic effect in the gas detection was observed. Only a few reported articles on P4VP in gas sensing [20].

This work introduces poly-4-(vinylpyridine) on MnO_2 nanorods-carbon nanoparticles composite to form a ternary composite to improve sensing properties. MnO_2 NRs-CNPs-P4VP composite sensors are used to detect ethanol vapour at room temperature. Initially, a ratio of 1:1 will be used to make a composite of MnO_2: CNPs composite sensor and be evaluated in gas sensing. To improve sensitivity, a mass equivalence of 1, 2, and 3 mass ratio will be added into a material 1:1 mass ratio of MnO_2:CNPs to investigate a composition that improves sensitivity towards detecting VOCs. After the mass ratio of the polymer is found, the change in the mass ratio (1, 2 and 3) of MnO_2 within the ternary composite will be studied.

2. Experimental section

2.1. Reagents and materials

Lighthouse candles that were used to prepare carbon soot were purchased at our local supermarket (Shoprite). Potassium permanganate (99.0 %), manganese sulphate monohydrate (98.0), poly-4-vinylpyrridine (99.5 %), N-N-dimethylformamide (99.8 %), ethanol (99.8 %), 2-propanol (99.5 %), methanol (99.9 %), mesitylene (99.5 %), and acetone (99.5 %) were all purchased at Sigma Aldrich, South Africa.

2.2. Preparation of carbon soot

Carbon nanoparticles, commonly known as carbon soot, are prepared via pyrolysis. In brief, the carbon soot was prepared by placing a ceramic cup on top of the (~2 cm) burning lighthouse candle in the presence of atmospheric air. A ceramic cup with soot was cooled at room temperature after collection and scraped and stored in a vial until further use [3].

2.3. Synthesis of MnO_2

The MnO_2 nanorods (NRs) were synthesised using the hydrothermal method J. Zhang et al. reported [4]. Firstly, 0.63 g of $KnMO_4$ and 0.25 g $MnSO_4.H_2O$ were dissolved in 40 mL of deionised water. The resulting solution was stirred for 30 min to obtain a homogeneous purple solution. The solution was transferred into a 100 mL Teflon-lined stainless steel autoclave, and the hydrothermal process was carried out at 160 °C for 12 h. After the reaction was completed, the autoclave was allowed to cool to room temperature, and the dark brown precipitate was washed several times with deionised water and ethanol by centrifugation and dried at 80 °C [11].

2.4. Sensor fabrication

All the sensors were prepared on a gold-plated interdigitated electrode that is designed to have 18 pairs of gold lines having 0.1 mm with a spacing between and each line is 7.9 mm long. The designs were done on an insulated substrate. All the electrodes were cleaned with ethanol and DMF several times and dried at room temperature. MnO_2 NRs, CNPs, MnO_2 NRs-CNPs-P4VP composites were used as sensing materials to prepare five sensors; sensor 1 (MnO_2 NRs), sensor 2 (CNPs), sensor 3 (CNPs-P4VP composite with a mass concentration of 10 mg:30 mg), sensor 4 (MnO_2 NRs-CNPs-P4VP composite with a mass concentration of 10 mg:10 mg:30 mg) and sensor 5 (MnO_2 NRs-CNPs-P4VP composite with a mass concentration of 30 mg:10 mg:30 mg) (see Table 1). The respective materials for each sensor were dissolved and physically mixed separately in DMF contained in vials. The mixed solutions were drop-coated onto a gold-plated interdigitated electrode, and the film was allowed to dry at room temperature. Further, the sensors were kept in a vacuum desiccator for about seven days to remove all the remaining DMF on the film.

2.5. VOCs tested and gas sensing measurement setup

The VOCs that were tested include methanol, ethanol, acetone, 2-propanol, and mesitylene vapours. The vapour concentrations were calculated using the formula [3].

$$C = \frac{22.4pTVs}{273MrV}\ 1000 \tag{1}$$

where C is the vapour concentration (ppm), p is the density of the liquid analyte ($g.cm^{-1}$), T is the temperature (K), Vs is the volume injected into the 20 L volumetric flask (μL), Mr is the molar mass of the liquid analyte and V is the volume of the volumetric flask (L). All sensors were tested using the same sensing setup under the resistance parameter. A sensor connected to the E4980A keysight LCR meter was placed inside a 3-necked 20 L round bottom flask (see Fig. 1). The measurement was done at 0.5 V AC and 25 kHz [11]. The round bottom flask (sensing chamber) has an opening for a pipe connected to a vacuum pump to remove gas from inside the chamber and it also has a pipe to introduce some external fresh air. Five trials of 1, 2, 3, 4 and 5 μL of VOC of interest were injected into the round bottom flask for each volume with contact time of 10 min; subsequently, the exposed VOCs were removed using a vacuum pump for 2 min at atmospheric pressure and a rest period of 3 min was done before the next injection. The liquid analytes evaporate easily due to their high vapour pressure and low boiling point.

2.6. Sensor response and recovery tests

The response time is the time taken by the sensor to reach the plateau of the maximum response. The time taken by the sensor to return to its baseline during analyte vapour removal from contact with the sensor is referred to as recovery time. In this study, the response time was recorded as 90 % of the maximum response when the analyte was in contact with the sensor, and the recovery time was measured as 90 % before the sensor reached its baseline. The electrical responses of the prepared sensors to the target gas were reported as the relative resistance (ΔR) and defined as

$$\Delta R = R_{gas} - R_{air} \tag{2}$$

2.7. Selectivity test

Firstly, 1 mL of each of the five analytes (ethanol, methanol, acetone, 2-propanol, and mesitylene) were mixed to make 5 mL. A 5 μL of aliquot from the mixture were tested to investigate the selectivity of ethanol vapour detections using the setup presented in Fig. 1.

2.8. Humidity test

Our sensor was tested at room temperature under different humid conditions. With the sensor present, boiled water vapour was controllably transferred into our 20 L round bottom flask. The volatile organic compound of interest was injected in that selected humidity, and the response was recorded.

Table 1
The prepared sensors and their respective mass ratios.

Sensor name	Sensing material	Mass (mg)	Mass ratio
Sensor 1	MnO_2	10	1
Sensor 2	CNPs	10	1
Sensor 3	CNPs-P4VP	10:30	1:3
Sensor 4	MnO_2-CNPs-P4VP	10:10:30	1:1:3
Sensor 5	MnO_2-CNPs-P4VP	30:10:30	3:1:3

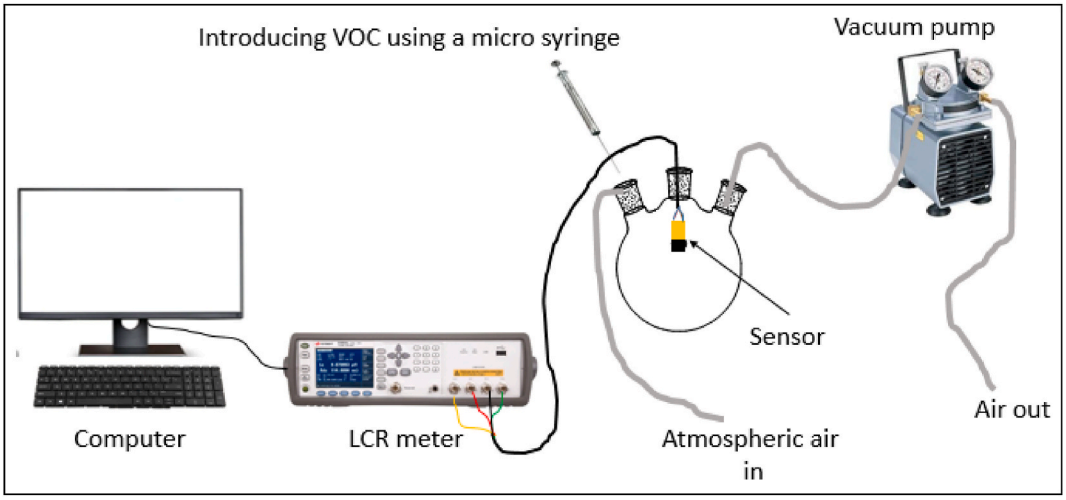

Fig. 1. Gas sensing setup.

2.9. *In Situ FTIR coupled with LCR meter setup and testing*

The prepared sensor was positioned on the upper wall of a 110 mL cylindrical gas cell and sealed on both ends with KBr windows. An LCR meter was electrically connected to the sensor. The IR beam entered the cell through KBr windows, which sealed it off and was positioned in the middle of the FTIR sample compartment. Before the gas analyte was injected into the gas cell, a pre-injection period of approximately 180 s was spent running the sensor. During the *in situ* measurement, approximately 20 ppm of ethanol vapour was introduced into a cylindrical cell. The LCR meter measured the sensor's electrical response (resistance), and the FTIR was used to record the IR spectra of the ethanol vapour during its interaction with the operating sensor. The total FTIR spectra recorded were 20 in number and each FTIR spectrum was recorded every 2 min. The same gas sensing setup was followed as referenced for the in-situ LCR meter connected to FTIR experiment [11,21].

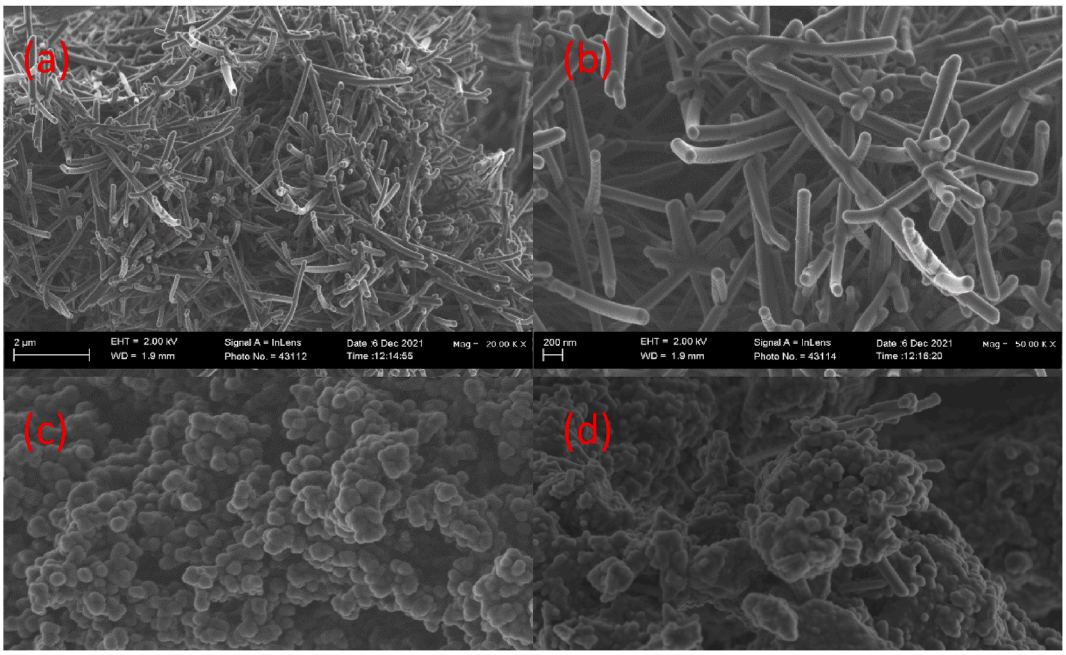

Fig. 2. SEM images of (a–b) MnO_2 NRs, (c) CNPs and (d) MnO_2 NRs-CNPs-P4VP composite.

2.10. Curve fitting for the infrared CO_2 band

Magic plot software was utilised to determine the area under the curve in a specific region of the CO_2 band that bends at around 668 cm^{-1} on the infrared bands. A Gaussian function was used to calculate the area under the curve of the CO_2 IR band.

2.11. Characterisation techniques

Morphologies of the synthesised materials were analysed on a JEOL-TEM 2010 (Japan) transmission electron microscope (TEM) at an acceleration voltage of 200 kV using the Gatan software. the TEM samples were prepared by dispersing the solid sample in ethanol and DMF (1:3) and then drop-coated onto copper grids coated with Holey carbon. Before mounting the sample, the sample was left to dry on the Holey carbon-coated copper. Utilising an FEI Nova Nanolab 600 FEG-SEM, scanning electron microscopy (SEM) was conducted at 30 kV. Structural analysis was revealed using powder X-ray diffraction (PXRD), Bruker D2 Phaser using LynxEye detector with radiation of a CuKα at a wavelength of 0.154 nm and Bruker Senterra laser Raman spectrometer fitted with frequency-doubled

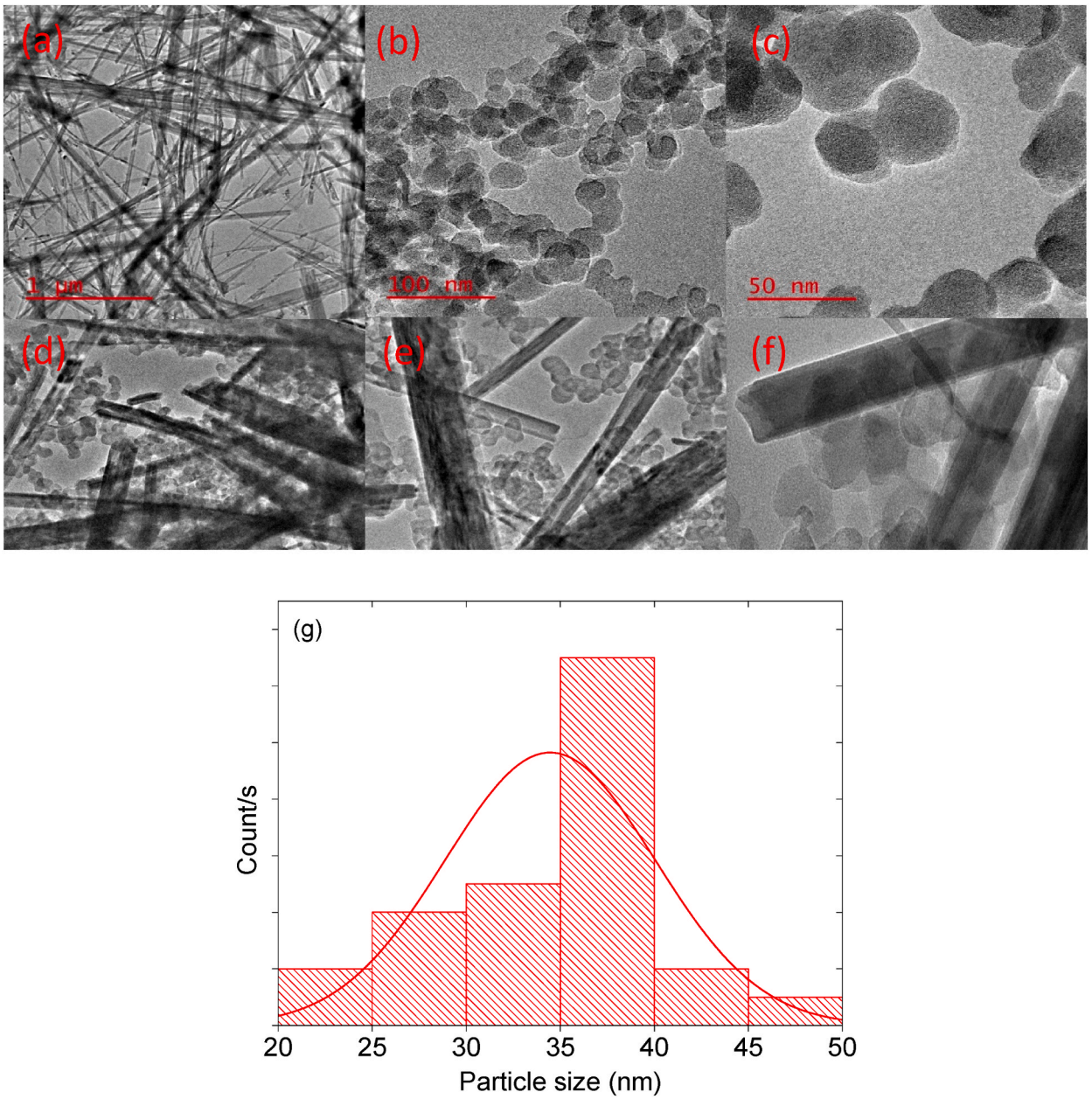

Fig. 3. TEM images of (a) MnO_2 NRs, (b–c) CNPs, (d–f) MnO_2 NRs-CNPs-P4VP composite and the particle size distribution of the CNPs.

Nd-YAG laser with the wavelength of 532 nm. Fourier transform infrared spectroscopy (FTIR, PerkinElmer Spectrum 100) was used to determine the sensing mechanism and characterise the materials by studying their functional groups. Solid samples weighing approximately 5 mg were combined with 0.8 g of potassium bromide (KBr) to prepare the mixture sample. A pestle and mortar were used to grind the mixture sample, and the pressed pellet method was used to produce the FTIR solid pellet.

3. Results and discussions

3.1. Material characterisation

Scanning electron microscopy (SEM) was used to study the external morphologies of the synthesised MnO_2 NRs, CNPs, and MnO_2 NRs-CNPs-P4VP composite. The hydrothermally prepared MnO_2 comprises nanorods with an average diameter of 138 nm. The MnO_2 nanorods are smooth in texture and uniform and appear disoriented (see Fig. 2a and b). The SEM image clearly showed the agglomerated spherical CNPs successfully prepared from the pyrolysis of lighthouse candles (see Fig. 2c). The MnO_2 NRs, CNPs, and P4VP mixture show a rough surface. Poly-4-(vinylpyridine) worked as a binder to hold and fuse the MnO_2 NRs and CNPs, forming microstructures to improve the electron mobility within the materials, resulting in a good sensitivity sensor (see Fig. 2d).

TEM is the microscopic technique used to reveal the internal morphological arrangements of the prepared materials (see Fig. 3). The TEM images shown in Fig. 3a revealed that the MnO_2 are nanorods with an average diameter of about 106–156 nm, which is close to the SEM to calculate the average diameter and the rods are randomly mixed. The CNPs are spherical agglomerated particles with an average particle diameter of 35 nm and are not uniform. The CNPs are stacked on one another, forming chain-like structures (see Fig. 3b and c). TEM images displayed in Fig. 3d–f reveal that P4VP made an adhesive layer that holds the manganese oxide nanorods and carbon nanoparticles to distribute the particles attached evenly. The average particle size of CNPs was found to be 35 nm, as shown in Fig. 3g.

PXRD patterns of CNPs, MnO_2 NRs, P4VP, and MnO_2 NRs-CNPs-P4VP composite are shown in Fig. 4. The XRD pattern of CNPs shows two broad peaks situated at $2\theta = 24.1^\circ$ and 44° attributed to (002) and (101) for crystal faces of graphitic carbon [ICDD: 04-018-7559]. For the MnO_2, the XRD patterns occurring at $2\theta = 12.7^\circ$, 17.9°, 25.6°,28.6°, 37.4°, 41.8°, 49.8°, 56.1°, 60.1°, 65.4°, 69.5°, and 72.9° are assigned for crystal planes (110), (200), (220), (310), (211), (301), (411), (600), (521), (002), (541) and (222) are indexed to tetragonal structure of α-MnO_2 [JCPDS No. 44–0141], and the previous studies found similar findings [22,23]. The P4VP XRD pattern shows a broad peak positioned $2\theta = 24.5^\circ$ is designated as the crystallinity of the polymer (see Fig. 4) [24]. The XRD patterns of MnO_2 NRs-CNPS-P4VP show a broad peak of the P4VP and multiple peaks from the MnO_2. However, the two peaks of CNPs are not visible due to low intensity compared to P4VP and MnO_2 NRs.

Raman spectroscopy (see Fig. 5a) and FTIR (see Fig. 5b) were used to study vibrational bond modes of CNPs, MnO_2 NRs, P4VP, and MnO_2 NRs-CNPs-P4VP. The Raman of CNPs exhibits two broad bands positioned at 1345 and 1592 cm^{-1}, ascribed to D and G bands, in an orderly fashion. The presence of the D bands represents the disorganised lattice arrangements of CNPs, while the G band is attributed to the sp^2 arrangements (graphitic nature) of the CNPs. The I_D/I_G ratio of CNPs was calculated by calculating the integrated intensity ratio between the D and G bands, which was 1.08, indicating the presence of oxygen species on the carbon nanoparticles [25]. The Raman spectrum of MnO_2 NRs shows a peak at 641 cm^{-1} attributed to O-Mn-O stretching vibration and MnO_6 octahedral vibrational units commonly known as fingerprints of α-MnO_2 fingerprints. The small peak positioned at 356 cm^{-1} is due to the laser

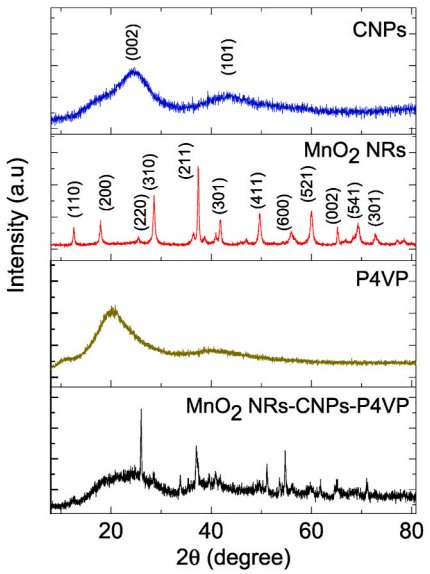

Fig. 4. PXRD patterns of CNPs, MnO_2 NRs, P4VP and MnO_2 NRs-CNPs-P4VP composite.

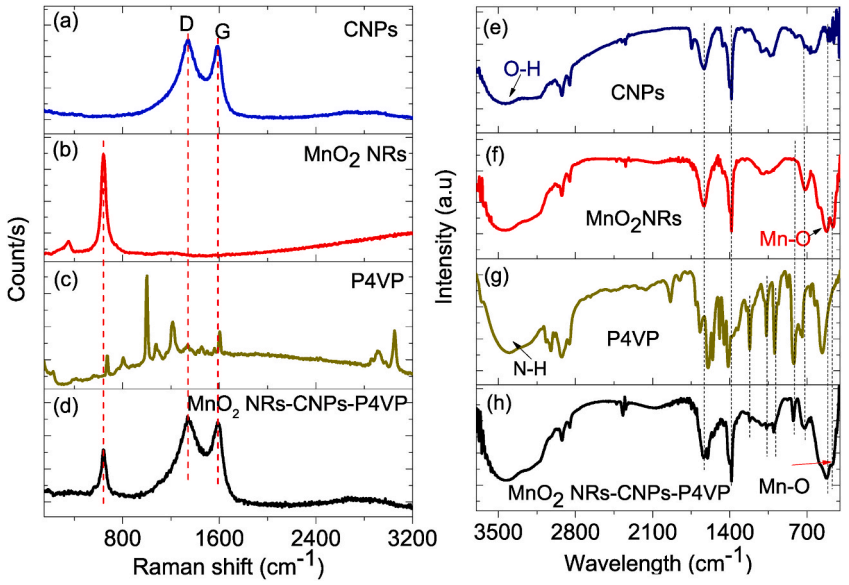

Fig. 5. Raman spectra of (a) CNPs, (b) MnO_2 (c) P4VP, (d) MnO_2 NRs-CNPs-P4VP and FTIR spectra of (e) CNPs, (f) MnO_2 NRs, (g) P4VP, and (h) MnO_2 NRs-CNPs-P4VP composite.

exposure of α-MnO_2 to form Mn_2O_3 [26–28]. Raman's spectrum of P4VP showed peaks at 2957 and 3057 cm-1 ascribed for C-H stretching in-plane on the aromatic ring in-plane, the peak positioned at 1608 cm^{-1} assigned to C=C stretching on the vinyl group. The Raman peak at 1454 cm^{-1} confirms the C=N on the pyridine group. A strong peak positioned at 1001 cm^{-1} is assigned to C-C stretching on the aromatic ring, and a peak of 667 cm^{-1} confirms the C-H stretching out of the plane on the aromatic ring [29–31]. The Raman spectrum of MnO_2 NRs-CNPs-P4VP confirms the presence of MnO_2 NRs shown by the intense on 641 cm^{-1}, the CNPs (D and G bands) and there are no displayed Raman peaks of P4VP moiety, which are due to the dominance of MnO_2 NRs, and CNPs Raman peaks.

The CNPs FTIR spectrum is displayed in Fig. 5a, showing a pronounced peak positioned at 3555 cm^{-1} assigned to O-H stretch. The two peaks at 3232 cm^{-1} and 2906 cm^{-1} represent C-H stretch and the peaks occurring at 1645 cm^{-1}, 1388 cm^{-1} and 1105 cm^{-1} are for H-O-H and C=O stretching, C-OH stretching, C-O bend stretch [21]. The MnO_2 NRs FTIR spectrum depicted peaks at 3232, 1606, and 1387 $cm^{-1,}$ revealing the moisture present in the compound and peaks at 521 and 452 cm^{-1} assigned for Mn-O and Mn-O-Mn stretchings confirming the presence of α-MnO_2 structure (see Fig. 5b) [12,32,33]. The FTIR spectrum of P4VP exhibits peaks at 3395, 2937, 1945, 1211, and 819-1399 cm^{-1} are assigned for N-H stretching, C-H stretching on the alkyl group, C=N stretching from the pyridine group, C-N stretching, and C-H stretching. There are traces of moisture on the compound, characterised by a peak occurring at 1622 cm^{-1} [34]. The FTIR spectrum of the composite proved the existence of α-MnO_2 NRs by depicting the pronounced Mn-O peak, CNPs, and P4VP peak traces in the MnO_2 NRs- CNPs-P4VP.

3.2. Gas sensing application

3.2.1. Sensors' response, sensitivity and selectivity

The electrical responses were studied during the vapour contact of the analytes and the prepared sensors, operated at room temperature. The analytes tested include 2-propanol, acetone, methanol, ethanol, and mesitylene vapours. The selectivity and sensitivity of the fabricated sensors were studied during the testing. Sensitivity (Ω ppm^{-1}) is defined as "S" = $\Delta R/\Delta C$, where S represents sensitivity, ΔR is the change in electrical response R= R_{gas}–R_{air} (measured in Ω), and ΔC is the change in concentration (ppm^{-1}). Sensor 1 (made up of only CNPs) showed weak sensing responses on all the analytes; linear relationships between resistance responses and analyte concentrations were not observed; the sensor fails to show an increase in gas response as the vapour concentration of the analytes increases (see Fig. S.1). Carbon soot (CNPs) sensor responded to all the tested vapours because of the oxygen availability on the surface. Even the Raman analysis showed that the CNPs are highly disordered (see Fig. 6a) and the CNPs have high charge activity transfer that effectively facilitates the chemisorption of ethanol [11,14]. Sensor 1 shows a low signal-to-noise ratio, which makes it difficult to measure response and recovery times. However, sensors 2 (MnO_2 NRs-CNPs) and sensor 3 (CNPs-P4VP) were fabricated and tested to improve the drawbacks possessed by sensor 1. Although the binary composite sensors did not show good sensing patterns (see Fig. S.2), they showed an increase in gas sensing response compared to CNPs alone and showed inconsistent responses. The failure to possess good sensing responses of vapours from single and binary materials made sensors that operate at room temperature allowed the introduction of ternary composites, materials, namely MnO_2 NRs, CNPs, and P4VP to fabricate sensors 4 and 5; therefore the mass of MnO_2 NRs within the ternary composite was varied to investigate the effect of the MnO_2 NRs on the sensitivity and selectivity, the response and recovery time of the sensors with the analytes. Thus, after exposing the sensors, sensor 4 (MnO_2

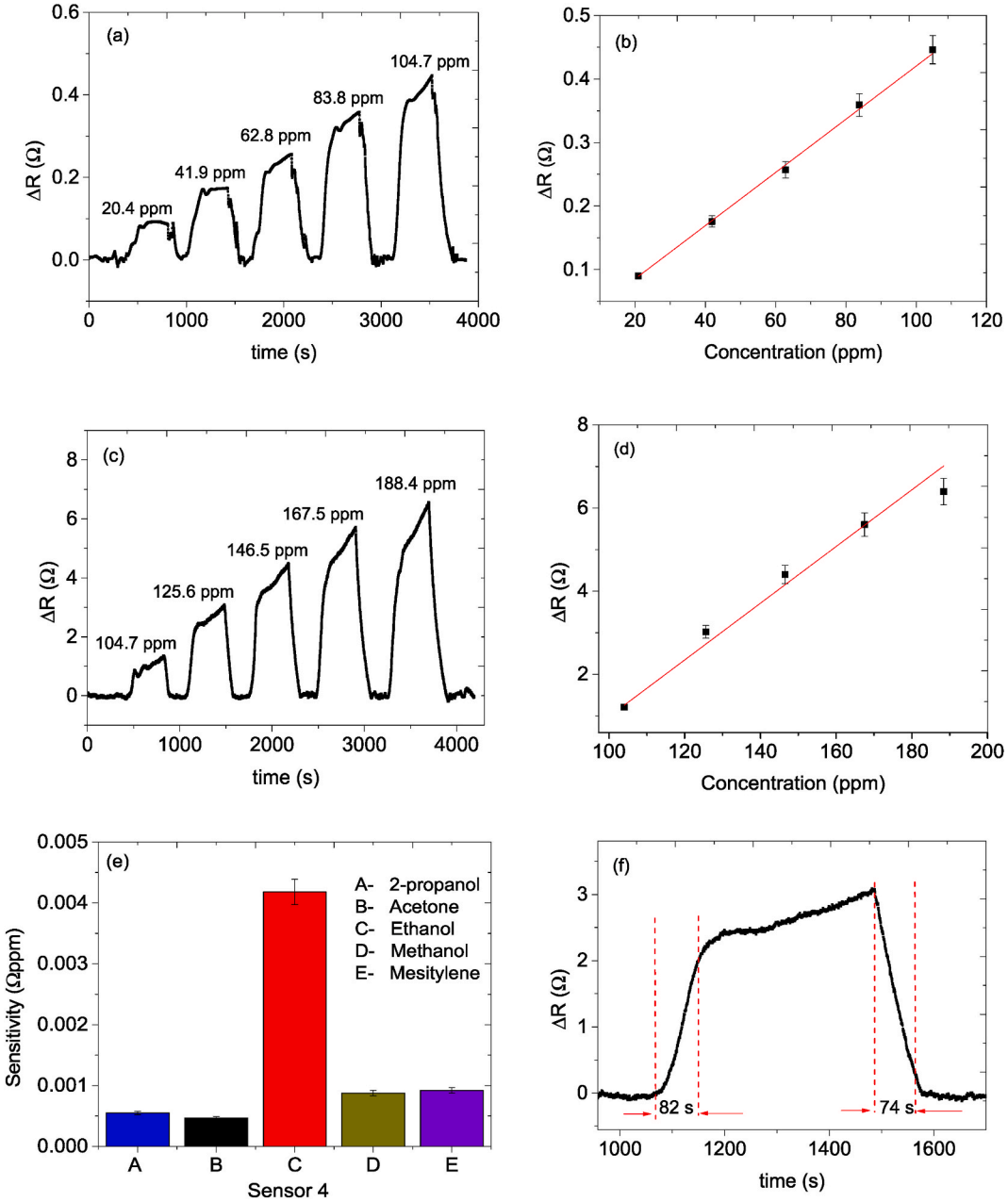

Fig. 6. Dynamic relative resistance response curve of sensor 4 (a) on ethanol vapour at concentration from 20.4 to 104.7 ppm, (b) its calibration curve (c) on ethanol vapour at concentration from 104.7 to 188.4 ppm, (d) its calibration vapour, (e) VOCs sensitivity bar graph of sensor 4 and (f) response-recovery time graph of toluene vapour on sensor 4.

NRs-CNPs-P4VP mass ratio 1:1:3) showed good sensing responses towards ethanol vapour (see Fig. 6a–d). Sensor 4 is highly sensitive towards ethanol vapour (0.00418 Ω ppm^{-1}) and poor sensitive to acetone (0.000467 Ω ppm^{-1}), 2-propanol (0.000549 Ω ppm^{-1}), methanol (0.000874 Ω ppm^{-1}) and mesitylene (0.000919 Ω ppm^{-1}) vapours. Sensor 5 (mass ratio 3:1:3) showed improvement in gas response magnitude in all the analytes but did not show meaningful results as the sensor failed to show an increase in gas response as the gas concentration increased. Among all the five prepared sensors, sensor 4 is the best sensor for detecting ethanol vapour. Sensor 4 was tested at lower concentrations ranging from 20.4 ppm to 104.7 ppm and also tested at higher concentrations ranging from 104.7 ppm to 188.4 ppm (see Fig. 6a and b) and interestingly, it showed good sensing behaviour with a consistent increase in electrical responses as the analyte concentration increased.

Furthermore, the response and recovery times for sensor 4 were also determined, which were approximately 82 s and 74 s, respectively (see Fig. 6f). The response slower than the recovery, which could be mainly due to the diffusion of the analyte vapour

through the composite sensing film and when diffusion rate is slower, the sensors take longer to respond [35–38].

3.2.2. *Repeatability and effect of humidity investigations of sensor 4*

(a) Repeatability investigations

The ability of the sensor to reproduce the same reading to the same concentration over time was studied by injecting 125.6 ppm ethanol into a 20 L round bottom flask for five cycles (see Fig. 7a). The depicted repeatability curves showed good stability, regenerate ability, and reproducibility of sensor 4 towards ethanol vapour detection at room temperature (see Fig. 7a and b). The individual resistance response values of the five tested cycles of ethanol vapour at 125.6 ppm was 3.09 Ω, 2.99 Ω, 3.07 Ω, 2.92 Ω, and 2.92 Ω (see Fig. 7a). The average response was 2.998 ± 0.0719 Ω, indicating that the sensor repeatedly read the value for the same concentrations.

(b) Effect of relative humidity on the performance of the sensor

Humidity is a crucial factor that negatively affects the sensor's performance; therefore, a solid-state sensor is needed to resist humidity. Some other solid-state gas sensors are responsive to a steady increase in humidity; thus, the vapour response can be suppressed. For this test, we used a 125.5 ppm of ethanol vapour concentration to test the sensor at different relative humidities, i.e. 37 %, 48 %, 55 %, and 72 % RH. The maximum response of sensor 4 during the exposure to 125.6 ppm ethanol vapour at different humidity conditions (37 %, 48 %, 55 %, and 72 % RH) was 3.25 Ω, 3.96 Ω, 3.87 Ω, and 5.11 Ω, respectively (see Fig. 7c). The response curve shapes of ethanol vapour detection at different humidity conditions remained the same; however, the ethanol vapour response increases as humidity in the chamber increases. There is about 25 % change in relative electrical resistance response from 37 % to 72 % relative humidity, but there is an approximately 10 % change in ethanol vapour response as the humidity changes from 37 % to 55 % RH; the sensor's response was high, which means the humidity affect the sensor's response; this is due to the P4VP is a hydrophobic polymer, the sensor is resistant to humidity change during ethanol vapour detection [35], therefore, the sensor can less affected below RH is 55 %. Interestingly, relative humidity increase slowed the sensor's response time (see Table 2 and Fig. 7c). The delay in ethanol vapour response might be competition between water molecules and the ethanol vapour for active sites on the sensing material and

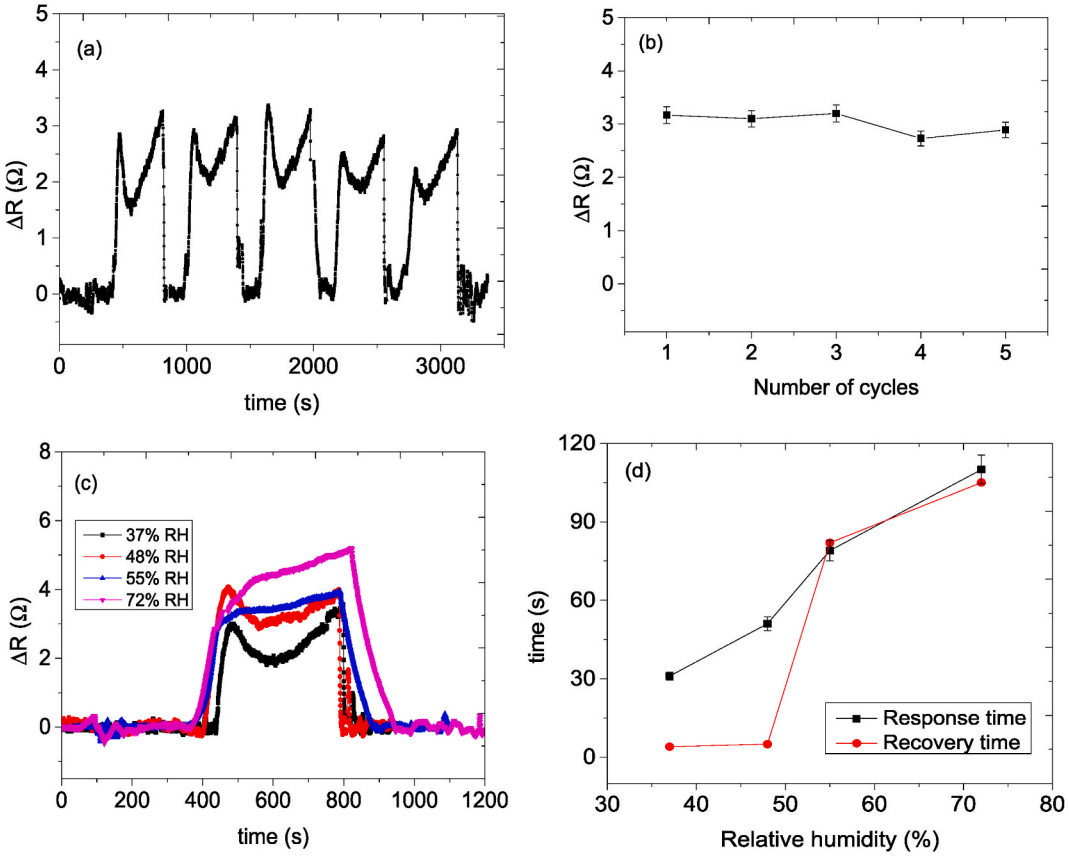

Fig. 7. (a) Repeatability graph, (b) its maximum response, (c) ethanol vapour response at different humidity conditions, and (d) response-recovery times at different humidities.

Table 2
Response and recovery times of methanol vapour on sensor 4 at different humidity conditions.

Relative humidity (RH)	Response time (s)	Recovery time (s)
37 %	31	4
48 %	51	6
55 %	82	82
72 %	79	105

similar results were reported [39]. Thus, the diffusion rate of the ethanol vapour on the sensor becomes slower at higher humidities. The slower recovery time might be a bond formation between the water molecules and the MnO_2 NRs since semiconductor metal oxide gas sensors are sensitive to humidity [40]. An increase in gas response during an increase in humidity on the sensors' surface could be from the co-adsorption of water molecules on the surface, which can play a crucial role as an electron acceptor. An increase in humidity results in the high surface distribution of hydroxyl (-OH) groups on the surface of the sensing material, increasing the sensing response. Thus, with relatively high humidity, the sensors' surface is covered with -OH groups, which limit oxygen adsorption. The released number of electrons from the water molecules is high compared to that of the targeted gas, which is why, in some cases, the response of the targeted vapour analyte is suppressed by the response of water molecules [41].

The MnO_2-CNPs-P4VP sensing material exhibits better ethanol sensing performances operating at room temperature than the reported ethanol sensors at higher temperatures (see Table 3).

3.2.3. Limit of detection

Knowing that the prepared sensor can detect the lowest possible concentration is very important. The gas sensor limit of detection (LOD) is the minimum vapour concentration the sensor can detect. To calculate the LOD, we considered a correlation coefficient (R^2) equal 0.99 and a gradient of 0.00418 Ω ppm^{-1} of sensor 4 (see Fig. 6b) and by definition LOD = 3 × RMS/slope [46], wherein the RMS is the standard deviation and RMS = 0.00011, hence, the LOD is 789 ppb. According to the result, our sensor can detect ethanol vapour with less than a ppm concentration (in ppb level).

3.2.4. Sensing mechanism

(a) General mechanism

The gas sensing mechanism of sensor 4 can be explained using gas adsorption-desorption processes. In this work, the MnO_2 NRs-CNPs-P4VP composite was made by using P4VP as a substrate binder and evenly loading the CNPs and MnO_2 NRs on the surface of the polymer. The improved sensing performance of MnO_2 NRs-CNPs-P4VP sensor to ethanol vapour compared to CNPs and non-responding materials P4VP and MnO_2 NRs could be that the materials form a heterojunction interface. The synergic effect could be that introducing CNPs in P4VP and MnO_2 NRs improves the number of active sites [47].

The atmospheric oxygens (O_2) are adsorbed on the surface of the sensing materials, then capture electrons from the conduction band and get ionised to form charged reactive oxygen species (O_2^-, O_2^{2-} and O^{2-}) [47]. The extraction of electrons from the conduction band forms an electron depletion layer, and as time progresses, the electron depletion layer changes the band to bend. Thus, the potential barrier is formed. During the sensing, the ethanol vapour reacts with reactive oxygen species on the surface of the sensor's active layer, forming carbon dioxide and water as by-products. After that, the trapped electrons were injected back into the sensing materials' conduction band, returning the bent band to its original state. The thickness or the width of the electron depletion layer slowly decreases, and the resistance of the active layer decreases, which is a typical behaviour of p-type SMO [48].

(b) The *in situ* FTIR coupled with the LCR meter study

The *in situ* FTIR coupled with the LCR meter was used to study the sensing mechanism. The FTIR spectra and LCR meter response were recorded during the ethanol exposure to the sensor placed inside the tight cylindrical cell (in the sample compartment of the

Table 3
Comparative analysis of previously reported ethanol sensors performance and our work.

Sensing materials	Concentration (ppm)	Res/rec time (s)	Relative response (Ω)	Temp (°C)	Ref
Co-doped SnO_2	200	16/5	49	300	[42]
WSe_2/RGO	100	15/10	5.5	180	[43]
MoO_2-Ni-graphene	100	150/179	54	25	[44]
α-MnO_2	100	–	1.53	180	[45]
MnO_2-PVP	345	97/32	11	25	[14]
MnO_2-CNPS-P4VP	20.4	82/74	0.1	25	**This work**

Not recorded (–)

FTIR) [49]. The FTIR spectra were recorded every 1 min for 20 min. The CO_2 IR band was studied to give evidence of the sensing mechanism (see Fig. 8). The *in situ* FTIR-LCR meter online shows a new peak at 668 cm^{-1}, which is assigned to the bending mode of CO_2 [11]. The intensity of the IR CO_2 peaks at 668 cm^{-1} increases as the time of ethanol exposure to the sensor increases; on the other hand, the intensity of C-H stretching peaks at 2900-3000 cm^{-1} decreases as the time of exposure increases (see Fig. 8b and c). The peak intensity of CO_2 mode and C-H stretching are inversely proportional to each other as the time of exposure increases; this means the ethanol vapour undergoes deep oxidation on the sensor's surface. In addition, the area under the curve of the CO_2 IR bands was plotted against the exposure time to understand the surface reaction. According to the result, the CO_2 intensity increases with increased sensor exposure time (see Fig. 9). Based on the results obtained from the *in situ* FTIR-LCR meter online analysis, it can be concluded that the sensor under the following reaction mechanism on ethanol vapour:

$$O_{2\ (gas)} \rightarrow O_{2\ (ads)} \tag{2}$$

$$O_{2\ (gas)} + e^{-} \rightarrow O_{2\ (ads)}^{-} \tag{3}$$

$$O_{2\ (ads)}^{-} + e^{-} \rightarrow 2O^{-}_{\ (ads)} \tag{4}$$

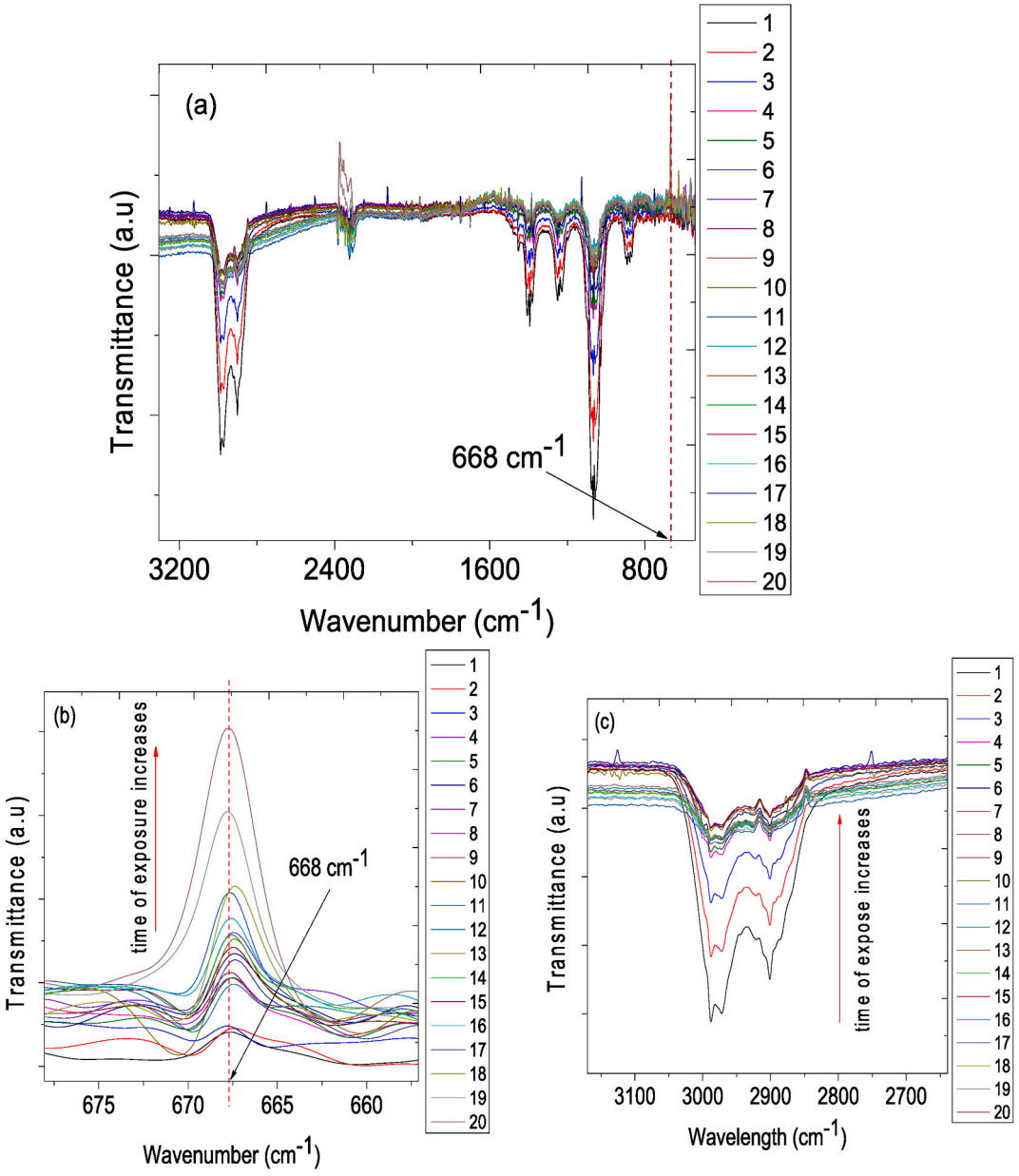

Fig. 8. (a) In *Situ* FTIR spectra of ethanol during sensing, (b) CO_2 IR band, and (c) C-H IR bands.

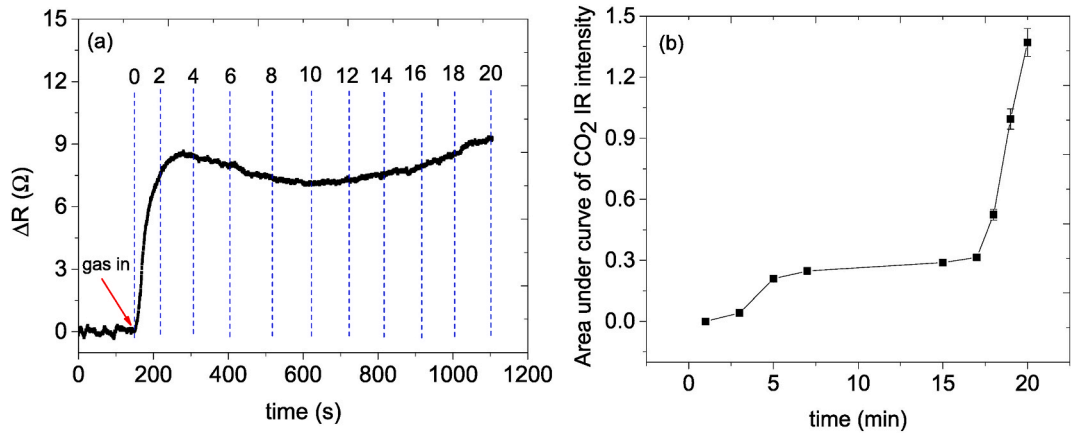

Fig. 9. (a) An ethanol vapour response from LCR during *in situ* studies, and (b) area under the curve of CO_2 IR intensity against time.

For ethanol vapour:

$$C_2H_6O\ (gas) + 7O^- \rightarrow 2CO_2 + 3H_2O + 7e^- \quad (5)$$

4. Conclusion

The successful synthesis and preparation of CNPs, MnO_2 nanorods, and MnO_2-CNPs-P4VP composite were confirmed by the characterisation techniques named SEM, HR-TEM, XRD, FTIR and Raman spectroscopy. The physical mixing method was opted to prepare the composites and the drop-casting method was used to prepare the solid-state gas sensors. All the sensing tests were done at room temperature the humidity effect was investigated. The prepared sensors: CNPs sensor, a sensor made up of 1:3 mass ratio of CNPs: P4VP, a sensor made up of the mass ratio 1:1:3 of MnO_2-CNPs-P4VP composite, and a sensor made up of the mass ratio 3:1:3 of MnO_2-CNPs-P4VP composite were exposed to various VOCs vapours. Among all the tested sensors, the sensor made up of a 1:1:3 mass ratio of MnO_2-CNPs-P4VP (sensor 4) composite was highly sensitive to ethanol and less sensitive to acetone, 2-propanol, mesitylene and methanol vapours. Sensor 4 had a fast response time of 51 s, and the recovery time of 6 s at the humidity of 48 % to ethanol vapour detection. Further, the online FTIR coupled with the LCR meter system has opted to study the sensing mechanism of the ethanol vapour on sensor 4, and it was found that it uses an adsorption-desorption mechanism wherein ethanol vapour is adsorbed on the sensing material and desorbed as water vapour and carbon dioxide gas.

CRediT authorship contribution statement

Lesego Malepe: Writing – original draft, Visualization, Methodology, Investigation, Formal analysis, Data curation. **Derek Tantoh Ndinteh:** Writing – review & editing, Supervision, Investigation. **Patrick Ndungu:** Writing – review & editing, Visualization, Supervision, Investigation. **Messai Adenew Mamo:** Writing – review & editing, Supervision, Project administration, Funding acquisition, Conceptualization.

Data availability

Data will be made available on request.

Declaration of competing interest

The authors declare that they have no known competing financial interests or personal relationships that could have appeared to influence the work reported in this paper.

Acknowledgements

This study was funded by the University of Johannesburg, South Africa.

Appendix A. Supplementary data

Supplementary data to this article can be found online at https://doi.org/10.1016/j.heliyon.2024.e40993.

References

[1] R. Shaik, R.K. Kampara, A. Kumar, C.S. Sharma, M. Kumar, Metal oxide nanofibers based chemiresistive H_2S gas sensors, Coord. Chem. Rev. 471 (2022) 214752.
[2] H.L. Li, H.Y. Zhan, S.Y. Fu, Rapid determination of methanol in black liquors by full evaporation headspace gas chromatography, J. Chromatogr. A. 1175 (2007) 133–136.
[3] L. Malepe, D.T. Ndinteh, M.A. Mamo, The effect of measurement parameters on the performance of the sensors in the detection of organic compound vapours, Chemical Physics Impact. 4 (2022) 100068.
[4] I. Piekarz, K. Wincza, S. Gruszczynski, J. Sorocki, Detection of methanol contamination in ethyl alcohol employing a purpose-designed high-sensitivity microwave sensor, measurement 174 (2021) 108993.
[5] N.A. Wright, L. Lee, Alcohol-related traffic laws and drunk-driving fatal accidents, Accid. Anal. Prev. 161 (2021) 106358.
[6] A.P. Pinheiro, J.M. Vedovoto, A.S. Neto, B.G.M. Van Wachem, Ethanol droplet evaporation: effects of ambient temperature, pressure and fuel vapor concentration, Int. J. Heat Mass Tran. 143 (2019) 118472.
[7] A. Nikfarjam, S. Hosseini, N. Salehifar, Fabrication of a highly sensitive single aligned TiO_2 and gold nanoparticle embedded TiO_2 nano-fiber gas sensor, ACS Appl. Mater. Interfaces 9 (2017) 15662–15671.
[8] F. Li, L. Chen, G.P. Knowles, D.R. MacFarlane, J. Zhang, Hierarchical mesoporous SnO_2 nanosheets on carbon cloth: a robust and flexible electrocatalyst for CO_2 reduction with high efficiency and selectivity, Angew. Chem. 129 (2007) 520–524.
[9] S. Wang, F. Jia, X. Wang, L. Hu, Y. Sun, G. Yin, T. Zhou, Z. Feng, P. Kumar, B. Liu, Fabrication of ZnO nanoparticles modified by uniformly dispersed Ag nanoparticles: enhancement of gas sensing performance, ACS Omega 5 (2020) 5209–5218.
[10] A. Umar, A.A. Ibrahim, R. Kumar, H. Algadi, H. Albargi, F. Ahmad, W. Zeng, M.S. Akhtar, α-MnO_2 Nanowires as potential Scaffolds for a high-performance Formaldehyde gas sensor device, Coatings 11 (2021) 860.
[11] V.O. Okechukwu, V. Mavumengwana, I.A. Hümmelgen, M.A. Mamo, Concomitant in situ FTIR and impedance measurements to address the 2-methylcyclopentanone vapor-sensing Mechanism in MnO_2—polymer nanocomposites, ACS Omega 4 (2019) 8324–8333.
[12] A. Umar, A.A. Ibrahim, R. Kumar, H. Albargi, W. Zeng, M.A.M. Alhmami, M.A. Alsaiari, S. Baskoutas, Gas sensor device for high-performance ethanol sensing using a-MnO_2 nanoparticles, Mater. Lett. 286 (2021) 129232.
[13] S. Mallakpour, F. Motirasoul, Bio-functionalizing of α-MnO_2 nanorods with natural l-amino acids: a favorable adsorbent for the removal of Cd(II) ions, Mater. Chem. Phys. 191 (2017) 188–196.
[14] G.E. Olifant, V. Mavumengwana, I.A. Hümmelgen, M.A. Mamo, Understanding the sensing mechanism of carbon nanoparticles: MnO_2–PVP composites sensors using in situ FTIR—online LCR meter in the detection of ethanol and methanol vapor, J. Mater. Sci. Mater. Electron. 30 (2019) 3552–3562.
[15] M. Morsy, I.S. Yahia, H.Y. Zahran, M. Ibrahim, Low cost Alcoholic Breath sensor based on SnO_2 modified with CNTs and graphene, J. Korean Phys. Society 73 (2018) 1437–1443.
[16] M. Morsy, I. Gomma, M.M. Mokhtar, H. ElHaes, M. Ibrahim, Design and implementation of humidity sensor based on carbon nitride modified with graphene quantum dots, Sci. Rep. 13 (2023) 2891.
[17] M. Morsy, A. Elzwawy, M. Oraby, Carbon nano based baterials and their composites for gas sensing applications: review, Egyptian journal of chemistry 65 (2022) 691–714.
[18] M. Morsy, I.S. Yahia, M. Ibrahim, Hydrothermal synthesis of CNTs/Co3O4@rGO mesopours nanocomposite as a room temperature gas sensor for VOCs, J. Inorg. Organomet. Polym. 29 (2019) 416–422.
[19] G.B. Pour, H.N. Fard, L. Fekri aval, P. Esmaili, Polyvinylpyridine-based electrodes: sensors and electrochemical applications, Ionics 26 (2020) 549–563.
[20] B. Yoon, S.F. Liu, T.M. Swagger, Surface-anchored Poly(4-vinylpyridine)–single-walled carbon nanotube–metal composites for gas detection, Chem. Mater. 28 (2016) 5916–5924.
[21] L. Malepe, D. Ndinteh, P. Ndungu, M.A. Mamo, Selective detection of methanol vapour from a multicomponent gas mixture using a CNPs/ZnO@ZIF-8 based room temperature solid-state sensor, RSC Adv. 12 (2022) 27094–27108.
[22] S.I. Shah, Zulfiqar, T. Khan, R. Khan, S.A. Khan, S.A. Khattak, G. Khan, Study of structural, optical and dielectric properties of α-MnO_2 nanotubes (NTS), J. Mater. Sci. Mater. Electron. 30 (2019) 19199–19205.
[23] D. Gangwar, C. Rath, Structural, optical and magnetic properties of α- and β-MnO_2 nanorods, Appl. Surf. Sci. 557 (2021) 149693.
[24] S.R. Jagtap, V.P. Raje, S.D. Samant, B.M. Bhanage, Silica supported polyvinyl pyridine as a highly active heterogeneous base catalyst for the synthesis of cyclic carbonates from carbon dioxide and epoxides, J. Mol. Catal. Chem. 266 (2007) 69–74.
[25] S. Perumbilavil, P. Sankar, T.P. Rose, R. Philip, White light scan measurements of ultrafast optical nonlinearity in reduced graphene oxide nanosheets in the 400–700 nm region, Appl. Phys. Lett. 107 (2015) 051104.
[26] S.I. Shah, S. Zulfqar, T. Khan, R. Khan, S.A. Khan, S.A. Khattak, G. Khan, Study of structural, optical and dielectric properties of α-MnO_2 nanotubes (NTS), J. Mater. Sci. Mater. Electron. 30 (2019) 19199–19205.
[27] V. Sannasi, K. Subbian, Influence of moringa oleifera gum on two polymorphs synthesis of MnO_2 and evaluation of the pseudo-capacitance activity, J. Mater. Sci. Mater. Electron. 31 (2020) 17120–17132.
[28] R. Roychaudhuri, D. Acharyya, P. Bhattacharyya, Morphological evolution of MnO_2 based nanostructures by tuning the reaction time, IEEE 17843467 (2018) 1–4.
[29] G. Pizarro, O.G. Marambio, M. Jeria-Orell, D.P. Oyarzun, R. Martin-Transco, J. Sanchez, Porous surface films with tunable morphologies and hydrophobic properties based on block copolymer under the effects of thermal annealing, Front. Chem. 7 (2019) 181.
[30] V.H. Pino, C. Alvarez-Lorenzo, A. Concheiro, E. Bucio, One-step grafting of temperature-and pH-sensitive (N-vinylcaprolactam-co-4-vinylpyridine) onto silicone rubber for drug delivery, Des. Monomers Polym. 20 (2017) 33–41.
[31] H. Nur, V.J. Cornelius, L.S. Benée, J.C. Mitchell, I.J. Day, M.J. Snowden, Semi-quantitative analysis of the monomer composition in co-polymer microgels using solid state Raman and NMR spectroscopy, Analyst. 134 (2009) 1366–1372.
[32] A. Yuan, X. Wang, Y. Wang, J. Hu, Textural and capacitive characteristics of MnO_2 nanocrystals derived from a novel solid-reaction route, Electrochim. Acta 54 (2009) 1021–1026.
[33] J.A. Lett, S.F. Alshahateet, I. Fatimah, R.P. Sivasankaran, A.K. Sibhatu, M. Le, S. Sagadevan, Hydrothermal synthesis and photocatalytic activity of Mn_3O_4 nanoparticles, Top. Catal. 66 (2022) 1–13.
[34] K. Mavronasou, A. Zamboulis, P. Klonos, A. Kyritsis, D.N. Bikiaris, R. Papadakis, I. Deligkiozi, Poly(vinyl pyridine) and its quaternized derivatives: Understanding their solvation and solid state properties, Polymers 14 (2022) 804.
[35] J.W. Gardner, M.Z. Iskandarani, B. Bott, Effect of electrode geometry on gas sensitivity of lead phthalocyanine thin films, Sens. Actuators, B 9 (1992) 133.
[36] J.W. Gardner, A non-linear diffusion-reaction model of electrical conduction in semiconductor gas sensors, Sens. Actuators, B 1 (1990) 166.
[37] K.C. Ho, Y.H. Tsou, Chemiresistor-Type NO gas sensor based on nickel phthalocyanine thin films, Sens. Actuators, B 77 (2001) 253.
[38] S. Kanaparthi, S.G. Singh, Reduction of the measurement time of a chemiresistive gas sensor using transient analysis and the cantor pairing function, ACS Meas. Sci. Au 2 (2022) 113.
[39] L. Malepe, D.T. Ndinteh, P. Ndungu, M.A. Mamo, A humidity-resistant and room temperature carbon soot@ZIF-67 composite sensor for acetone vapour detection, Nanoscale Adv. 5 (2023) 1956–1969.
[40] Y. Wang, L. Liu, F. Sun, T. Li, T. Zhang, S. Qin, Humidity-insensitive NO_2 sensors based on SnO_2/rGO composites, Front. Chem. 9 (2021) 681313.
[41] M. Shooshtari, A. Saleh, S. Vollebregt, Effect of temperature and humidity on the sensing performance of TiO_2 nanowire-based ethanol vapor sensors, Nanotechnology 32 (2021) 325501.
[42] Y. Tan, J. Zhang, Highly sensitive ethanol gas sensors based on Co-doped SnO2 nanobelts and pure SnO_2 nanobelts, Phys. E Low-dimens. Syst. Nanostruct. 147 (2023) 115604.

[43] A. Hussain, M.N. Lakhan, I.A. Soomro, M. Ahmed, A. Hanan, A.A. Maitlo, I. Zehra, J. Liu, J. Wang, Preparation of reduced graphene oxide decorated two-dimensional WSe_2 nanosheet sensor for efficient detection of ethanol gas, Phys. E Low-dimens. Syst. Nanostruct. 147 (2023) 115574.
[44] S. Mehmood, X. Zhao, M.F. Bhopal, F.U. Khan, Y. Yang, G. Wang, X. Pan, MoO_2-Ni-graphene ternary nanocomposite for a high- performance room-temperature ethanol gas sensor, Appl. Surf. Sci. 554 (2021) 149595.
[45] C. Liu, S.T. Navale, Z.B. Yang, M. Galluzzi, V.B. Patil, P.J. Cao, R.S. Mane, F.J. Stadler, Ethanol gas sensing properties of hydrothermally grown α-MnO_2 nanorods, J. Alloys Compd. 727 (2017) 362–369.
[46] O. Leenarrts, B. Partoens, F.M. Peeters, Adsorption of H_2O, NH_3, CO, NO_2, and NO on graphene: a first-principles study, Phys. Rev. B: Condens. Matter Mater. Phys. 77 (2008) 125416.
[47] Y. Yao, Z. Li, Y. Han, L. Xie, X. Zhao, Z. Zhu, Fabrication and characterisation of a $MnO_2/Ti_3C_2T_x$ based gas sensor for highly sensitive and selective detection of lung cancer marker hexanal, Chem. Eng. J. 451 (2023) 139029.
[48] A. Dey, Semiconductor metal oxide gas sensors: a review, Materials Science and Engineering B. 229 (2018) 206–217.
[49] L. Malepe, P. Ndungu, D.T. Ndinteh, M.A. Mamo, An in-situ FTIR-LCR meter technique to study the sensing mechanism of MnO_2@ZIF-8/CNPs and a direct relationship between the sensitivity of the sensors and the rate of surface reaction, Results in physics 52 (2023) 106864.